Stellar (n,γ) cross sections of neutron-rich nuclei: Completing the isotope chains of Yb, Os, Pt, and Hg

J. Marganiec*
Karlsruhe Institute of Technology (KIT), Campus North, Institute of Nuclear Physics, P.O. Box 3640, Karlsruhe, Germany and University of Lodz, Division of Nuclear Physics, Lodz, Poland

I. Dillmann,† C. Domingo-Pardo,‡ and F. Käppeler
Karlsruhe Institute of Technology (KIT), Campus North, Institute of Nuclear Physics, P.O. Box 3640, Karlsruhe, Germany
(Received 15 July 2014; published 1 December 2014)

The (n,γ) cross sections of the most neutron-rich stable isotopes of Yb, Os, Pt, and Hg have been determined in a series of activation measurements at the Karlsruhe 3.7 MV Van de Graaff accelerator, using the quasistellar neutron spectrum for $kT = 25$ keV that can be produced with the ^{7}Li$(p,n)^{7}$Be reaction. In this way, Maxwellian averaged cross sections could be directly obtained with only minor corrections. After irradiation the induced activities were counted with a HPGe detector via the strongest γ-ray lines. The stellar neutron capture cross sections of ^{174,176}Yb, ^{190,192}Os, ^{196,198}Pt, and ^{202,204}Hg, extrapolated to $kT = 30$ keV, were found to be 157 ± 6 mb, 114 ± 8 mb, 278 ± 11 mb, 160 ± 7 mb, 171 ± 19 mb, 94 ± 4 mb, 62 ± 2 mb, and 32 ± 15 mb, respectively. In the case of ^{196}Pt the partial cross section to the isomeric state at 399.5 keV could be determined as well. With these results the cross section data for long isotopic chains could be completed for a discussion of the predictive power of statistical model calculations towards the neutron-rich and proton-rich sides of the stability valley.

DOI: 10.1103/PhysRevC.90.065801 PACS number(s): 25.40.Lw, 27.50.+e, 28.20.Fc, 97.10.Cv

I. INTRODUCTION

Almost all elements are created during stellar evolution [1], the light elements up to iron by fusion reactions and the heavier elements predominantly by neutron capture processes. In the slow neutron capture process (*s* process), β^- decays are generally faster than the time between two consecutive neutron captures [2,3]. Accordingly, the *s* process advances along the valley of β stability, starting from the seed nuclei of the iron group and ending at the Pb isotopes and ^{209}Bi. Further neutron capture leads to ^{210}Bi, which β-decays to α-unstable ^{210}Po, thus recycling the reaction flow into the Pb isotopes. Depending on neutron exposure, three *s* components have been identified, the *weak*, *main*, and *strong s* process. The *s* abundances in the mass region between Fe and Sr ($A = 56$–90) are produced by the weak component in massive stars during core helium and shell carbon burning. Thermally pulsing low-mass asymptotic giant branch (TP-AGB) stars during their hydrogen shell burning phase and during helium shell flashes are the site of the main *s* component that contributes to the *s* abundances between Zr and the Pb/Bi isotopes ($A = 90$–209). About 50% of ^{208}Pb is accounted for by the strong component associated with AGB stars of low metallicity [4,5].

The isotopes ^{174}Yb, ^{190}Os, ^{196}Pt, and ^{202}Hg are part of the reaction path of the main *s* process. During this evolutionary phase, neutrons are produced via (α,n) reactions on ^{13}C and ^{22}Ne. The ^{13}C (α,n) reaction, which represents the main neutron source, operates during the H-burning periods before the subsequent He shell flashes under radiative conditions at temperatures of $T \sim 10^8$ K, corresponding to thermal energies of $kT = 8$ keV and neutron densities of $\sim 10^7$ cm^{-3}. At the higher temperatures reached during the He shell flashes ($kT = 25$ keV), the ^{22}Ne$(\alpha,n)^{25}$Mg reaction is activated and adds a second neutron exposure, which is characterized by peak neutron densities of $\sim 10^{10}$ cm^{-3}. The neutrons are quickly thermalized in the high-density stellar plasma resulting in an energy spectrum of Maxwell-Boltzmann type. The abundance distribution produced by the main *s* component is directly related to the Maxwellian averaged cross sections (MACS) of the involved isotopes, because the product of *s* abundances and the respective MACS values are constant in mass regions, where reaction flow equilibrium is reached [4].

The origin of the second group of the investigated isotopes, ^{176}Yb, ^{192}Os, ^{198}Pt, and ^{204}Hg, is commonly ascribed to the rapid neutron capture process (*r* process), because they are practically shielded from the *s* process by their short-lived neighbors. The *r* process occurs under explosive conditions, resulting in extremely high neutron densities in excess of 10^{20} cm^{-3}. In this case, the time between neutron captures is much shorter than the half-lives for β decay; consequently, the reaction path is shifted to the far neutron-rich region in the chart of nuclides, close to the neutron drip line. When the temperature drops and the neutron sources cease, the synthesized nuclei decay back to the valley of stability by β decays, adding to the abundances of the heavy elements up to Th/U. The *r* process is presumably associated with core collapse supernovae and/or neutron star mergers, but the astrophysical mechanism is not yet completely settled [6,7].

The role of (n,γ) cross sections in the *r* process becomes evident in the initial stages [8] as well as during the freeze-out phase when the free neutrons are captured by the predominantly unstable isotopes, which belong to the β-decay chains

*Corresponding author: TU Darmstadt, D-64291 Darmstadt, Germany; J.Marganiec@gsi.de
†Present address: TRIUMF, Vancouver BC, Canada.
‡Present address: IFIC, Valencia, Spain.

from the synthesis path back to stability. As the MACS data for these isotopes have to be inferred by theory it is important to test and to improve the predictive power of the reaction models used in this context. One possibility for such tests are the experimental MACS values for long isotope chains extending as far as possible to the neutron-rich side. So far, capture cross section measurements are limited to stable or very long-lived isotopes where enough material can be produced and backgrounds from the radioactivity of the sample can be managed. For more neutron-rich species indirect methods, e.g., Coulomb dissociation and surrogate techniques, or completely new concepts have to be considered [9].

The present activation measurements were motivated by discrepancies and sizable uncertainties of existing data at astrophysically relevant neutron energies as well as by the opportunity to study possible systematic differences with earlier time-of-flight (TOF) results. The activation technique has the advantage of excellent sensitivity and selectivity that allows one to determine the (n,γ) cross sections of several and even rare isotopes with samples of natural composition, because the individual reaction channels can be unambiguously separated by the characteristic γ decay of the product nuclei. Experiments and data analysis are described in Secs. II and III, and the results are presented in Sec. IV. Section V contains a comparison of the present MACS data with the latest evaluations and theoretical predictions.

II. EXPERIMENT

All measurements were carried out at the Karlsruhe 3.7 MV Van de Graaff accelerator using the activation technique. The method, which has been extensively used for s-process studies, consists of two steps, neutron irradiation of the sample in a well-defined neutron spectrum and the subsequent determination of the induced activity [10]. Because of our astrophysical motivation a quasistellar neutron energy distribution was used throughout this work.

A. Neutron spectrum

Neutrons were produced with the ^{7}Li$(p,n)^{7}$Be source by bombarding thin layers of LiF on a water-cooled Cu backing. With a proton energy $E_p = 1912$ keV, 30 keV above the reaction threshold, all neutrons are emitted into a forward cone of 120° opening angle and a maximum neutron energy of 106 keV (see Figs. 1 and 2). Neutron moderation is avoided because cooling is achieved by lateral heat conduction to a water channel outside of the neutron field. In this way, a quasi-Maxwellian neutron spectrum corresponding to a thermal energy $kT = 25.0 \pm 0.5$ keV can be closely approximated for the irradiations [10,11] as illustrated in Fig. 1. Accordingly, the proper stellar neutron capture cross section can be directly deduced from the measurements with only minor corrections.

The irradiation geometry shown in Fig. 2 was chosen such that the samples were entirely inside the conical neutron field. A ^{6}Li-glass detector at a distance of about 90 cm from the target served as a neutron monitor and was used for recording the time-dependence of the neutron flux, which decreases during the irradiations due to the degradation of the Li targets.

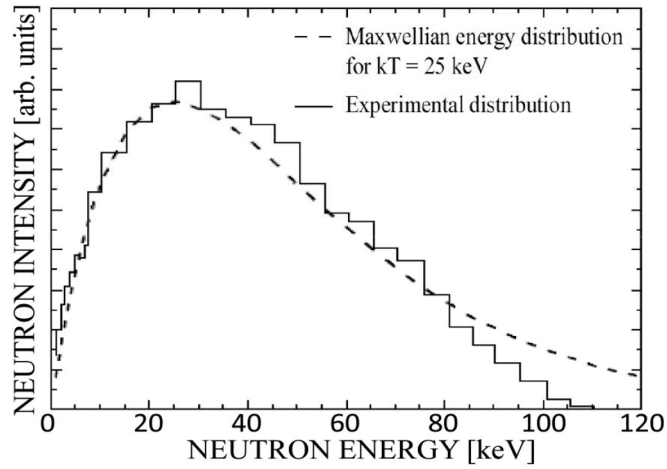

FIG. 1. Comparison of the experimental neutron energy distribution with Maxwellian distribution of $kT = 25$ keV [11].

B. Samples

The samples were pressed from oxides or chlorides of natural composition, except for Pt, which has been cut from a metal foil. The isotopic abundances have been adopted from Ref. [12]. Because the powders were potentially hygroscopic, adsorbed water was removed by heating the Yb_2O_3 and Hg_2Cl_2 samples to 500 °C and 300 °C, respectively. This procedure was not required for the OsO_2 sample because this material was certified and delivered in an airtight box.

In a series of activations the diameter and thickness of the samples as well as the irradiation times were systematically changed (Table I) in order to check for related systematic uncertainties. The irradiation times were chosen according to the half-lives of the respective product nuclei. The samples were sandwiched between two gold foils of the same diameter for normalization to the well-known (n,γ) cross section of ^{197}Au [11].

C. Irradiations

The irradiations were carried out with the accelerator operated in DC mode with beam currents between 80 and

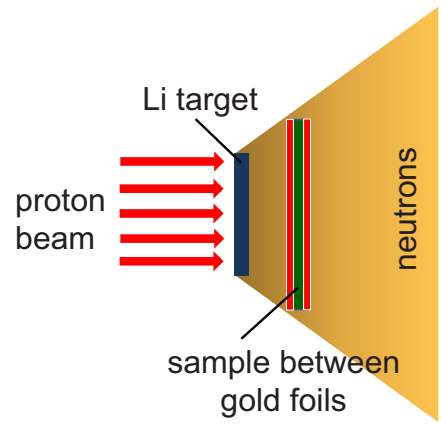

FIG. 2. (Color online) Schematic sketch of the experimental setup.

TABLE I. Sample characteristics, irradiation times, and integrated neutron flux Φ_{tot} for the 28 activations of this work.

Sample	Diameter [mm]	Thickness [mm]	Total mass [mg]	Activation time [h]	Φ_{tot} [10^{14}]
		^{174}Yb$(n,\gamma)^{175}$Yb			
Yb-1	10	0.55	399.69	88.37	2.44
Yb-2	10	0.53	382.89	62.95	2.17
Yb-3	10	0.42	300.96	64.87	1.57
Yb-4	10	0.30	215.90	62.08	1.76
Yb-5	6	0.50	131.54	61.35	0.94
Yb-6	6	0.47	122.07	69.20	1.36
		^{176}Yb$(n,\gamma)^{177}$Yb			
Yb-7	10	0.73	528.92	1.45	2.16
Yb-8	10	0.31	226.27	2.17	7.16
Yb-9	6	0.60	153.26	1.95	3.66
Yb-10	6	0.56	146.64	1.43	1.56
		^{190}Os$(n,\gamma)^{191}$Os, ^{192}Os$(n,\gamma)^{193}$Os			
Os-1	10	0.55	496.81	65.50	2.66
Os-2	6	0.61	197.19	43.83	1.52
Os-3	6	0.31	99.39	40.28	1.00
		^{196}Pt$(n,\gamma)^{197}$Pt			
Pt-1	10	0.02	37.94	54.95	2.18
Pt-2	6	0.08	46.38	54.70	0.98
Pt-3	6	0.05	30.80	34.67	0.56
		^{196}Pt$(n,\gamma)^{197m}$Pt, ^{198}Pt$(n,\gamma)^{199}$Pt			
Pt-1	10	0.02	37.94	1.25	0.037
Pt-2	6	0.08	46.38	1.30	0.030
Pt-4	10	0.05	75.84	1.29	0.041
		^{202}Hg$(n,\gamma)^{203}$Hg			
Hg-1	10	0.88	493.99	45.75	1.01
Hg-2	10	0.61	345.08	71.75	1.45
Hg-3	10	0.52	292.60	67.45	1.00
Hg-4	6	0.83	167.73	45.85	1.10
Hg-5	6	0.56	114.05	42.67	0.67
Hg-6	6	0.45	92.31	70.63	1.28
		^{204}Hg$(n,\gamma)^{205}$Hg			
Hg-7	10	0.94	529.21	0.17	0.0029
Hg-8	6	0.95	193.32	0.20	0.0022
Hg-9	6	0.61	123.73	0.18	0.0024

100 μA, yielding an average neutron intensity of $\sim 10^9$ s^{-1}. The effective integrated neutron flux seen by the samples was depending on the beam stability and the performance of the LiF targets. Throughout all irradiations the neutron flux was recorded with the ^{6}Li-glass monitor in time steps of 30 s. The time-dependence of the neutron flux is required to evaluate the proper correction for the fraction of product nuclei that decayed already during irradiation [expressed by the factor f_b in Eq. (5)]. The sample characteristics and the respective irradiation times are summarized in Table I for each of the 28 activations carried out in this work.

D. Induced activities

The induced activities were identified by means of well-shielded high-purity Ge (HPGe) detectors using the characteristic decay γ rays. The spectroscopic information for the decay properties of the various product nuclei are summarized in Table II.

TABLE II. Half-lives of product nuclei and related γ energies and intensities used in analysis.

Isotope	$t_{1/2}$	E_γ [keV]	I_γ [%]	Reference
^{175}Yb	4.185 (1) d	144.9	0.672 (10)	[13]
		282.5	6.13 (8)	
		396.3	13.2 (3)	
^{177}Yb[a]	1.911 (3) h	121.6	3.5 (4)	[14]
		150.3	20.5 (22)	
		1080.5	5.9 (5)	
		1241.8	3.5 (3)	
^{191}Os	15.4 (1) d	129.4	26.50 (4)	[15]
^{193}Os	30.11 (1) h	460.5	3.88 (5)	[16]
^{197}Pt	19.8915 (19) h	77.35	17.2 (24)	[17]
		191.4	3.7 (4)	
^{197}Pt^m	95.41 (18) min	346.5 (IT)	11.1 (3)	[17]
^{199}Pt[a]	30.8 (4) min	543.0	11.74 (10)	[18]
^{203}Hg	46.594 (12) d	279.2	81.56 (5)	[19]
^{205}Hg	5.14 (9) min	203.7	2.2 (10)	[20]
^{198}Au	2.69517 (21) d	411.8	95.58 (12)	[21]

[a]Isotopes with short-lived isomers, which decay with 100% probability by internal transitions (IT) to the ground state.

Depending on the induced γ intensities, three detector setups were used, two single HPGe detectors of 30% and 100% relative efficiency and a system of two HPGe Clover detectors with a relative efficiency of 130% each in very close geometry [22]. The single detectors were used in far geometry with a distance of 76 mm between sample and detectors. For all detectors, γ-energy and γ-efficiency calibrations were performed with a set of standard sources. In the relevant γ-energy range between 120–1480 keV the efficiencies were determined with an uncertainty of 2%. The γ efficiency of the HPGe Clover system was also simulated using the GEANT4 toolkit [23]. The simulations were required because some γ-ray lines lie outside the range covered by the calibration sources and also because the corrections for self-absorption and cascade summing, which are important in the close geometry of the Clover system could be determined in this way (see Sec. III). The efficiency curves are shown in Fig. 3.

The smaller HPGe detector was used for the higher activities, i.e., of the gold foils, as well as for the activities of ^{175}Yb (for two samples), ^{177}Yb, ^{191}Os, ^{193}Os, and ^{203}Hg. Intermediate activities (four ^{175}Yb samples and ^{205}Hg) were counted with the larger HPGe detector, whereas the HPGe Clover detection system was needed for the weak activities of isotopes with extremely low abundances or very weak γ-ray lines, i.e., ^{197}Pt, ^{197}Pt^m, and ^{199}Pt. Apart from the case of ^{205}Hg, γ-ray backgrounds were small and had practically no effect on the uncertainty of the final cross section values. Therefore, statistical uncertainties were much smaller than the respective systematic uncertainties.

The recorded γ-ray spectra are illustrated in Fig. 4, one taken with the smaller single HPGe detector showing the decay

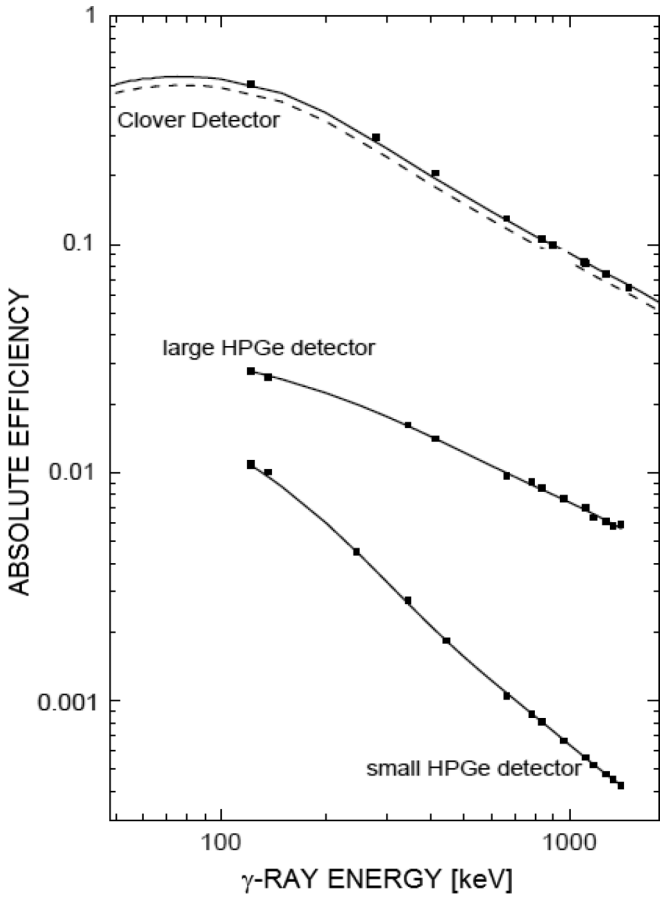

FIG. 3. Efficiency curves for the three HPGe detector setups used in the measurements. The dashed line for the Clover detector represents a GEANT4 simulation, which was normalized to the measured data points (black symbols and solid line).

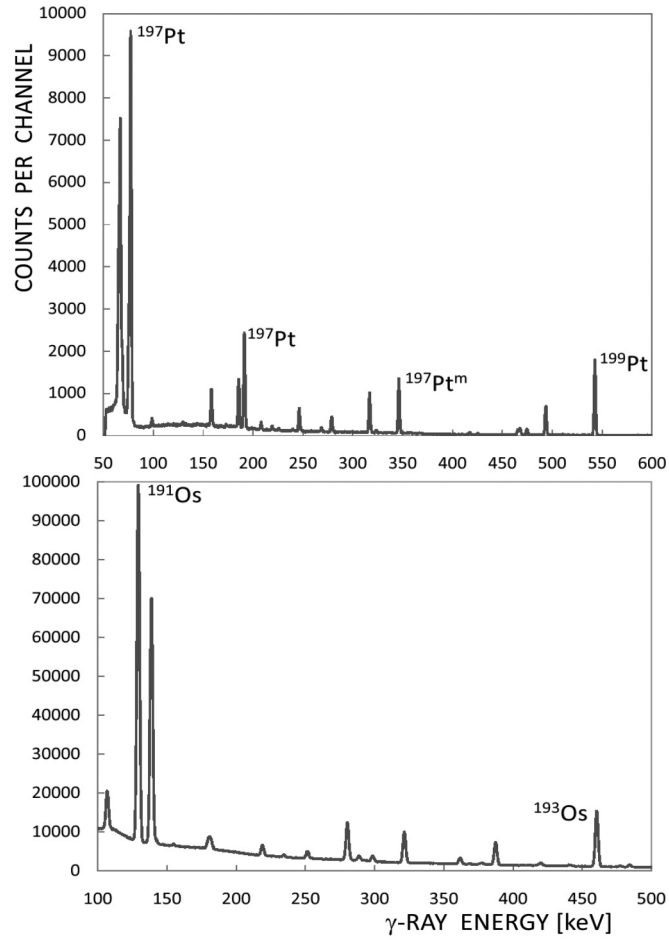

FIG. 4. Typical examples of γ-ray spectra taken with the HPGe Clover array after activation of sample Pt-1 (top) and with the smaller single HPGe detector after activation of sample Os-3 (bottom).

lines of ^{191}Os and ^{193}Os, and the example of Pt activations measured with HPGe Clover array.

III. DATA ANALYSIS

The total amount of activated nuclei A at the end of irradiation can be derived from the number of counts C in a particular γ-ray line registered in the HPGe detector during the measuring time t_m [10],

$$A = \frac{C}{K_\gamma \epsilon_\gamma I_\gamma (1 - e^{-\lambda t_m}) e^{-\lambda t_w}}, \quad (1)$$

where ϵ_γ denotes the detector efficiency, I_γ the intensity per decay, and t_w the waiting time between irradiation and activity measurement. The factor K_γ describes the γ-ray self-absorption in the sample. For disk samples one has [24]

$$K_\gamma = \frac{1 - e^{-\mu x}}{\mu x}, \quad (2)$$

where μ is the γ-ray self-absorption coefficient and x the sample thickness. This formula was a good approximation for measurements with the single HPGe detectors, because of the large distance between sample and detector. The respective γ-ray self-absorption coefficients μ were taken from Ref. [25]. For the close geometry of the HPGe Clover detectors, however, Monte Carlo simulations with the GEANT4 toolkit [23] were required instead, where the effect of photon scattering in the source had to be considered in evaluating the corrections for self-absorption and cascade summing.

The number of activated nuclei A can also be written as

$$A = \Phi_{\rm tot} N \sigma f_b, \quad (3)$$

where $\Phi_{tot} = \int_0^{t_a} \Phi(t) dt$ is the time integrated neutron flux and σ the spectrum averaged capture cross section (SACS). The sample thickness in atoms/cm^2 is

$$N = \frac{N_A m a}{M_A \pi R^2}, \quad (4)$$

where N_A denotes the Avogadro number, m the sample mass, R the sample radius, a the isotopic abundance, and M_A the molar mass.

The factor f_b in Eq. (3) corrects for the fraction of activated nuclei that decayed already during irradiation. By this correction nonuniformities in the neutron flux due to the decreasing performance of the LiF targets as well as fluctuations in the accelerator beam were properly taken

into account. While this correction is small or negligible for activation products with half-lives much longer than the irradiation time t_a, fluctuations in the neutron flux become important in cases where $t_{1/2} \approx t_a$. In the expression

$$f_b = \frac{\int_0^{t_a} \Phi(t) e^{-\lambda(t_a - t)} dt}{\int_0^{t_a} \Phi(t) dt}. \quad (5)$$

$\Phi(t)$ is the time-dependence of the neutron intensity recorded throughout the irradiation with the ^{6}Li glass monitor and λ the decay rate of the product nucleus.

As the measurements are carried out relative to the ^{197}Au reference cross section, the neutron flux $\Phi_{\rm tot}$ cancels out in the activity ratio

$$\frac{A_i}{A_{Au}} = \frac{\sigma}{\sigma_{Au}} \frac{N_i}{N_{Au}} \frac{f_{b_i}}{f_{b_{Au}}} \quad (6)$$

and the SACS σ_i becomes

$$\sigma_i = \frac{A_i}{A_{Au}} \cdot \frac{N_{Au}}{N_i} \cdot \frac{f_{b_{Au}}}{f_{b_i}} \cdot \sigma_{Au}. \quad (7)$$

The reference value for the experimental SACS of ^{197}Au in the quasistellar spectrum at $kT = 25$ keV is $\sigma_{Au} = 586 \pm 8$ mb [11].

For the far geometry used with the smaller HPGe detectors, the corrections for coincidence-summing and for the fact that the samples correspond to extended sources were calculated as described in Ref. [26] and were found to be negligible. In case of the Pt isotopes, which had been measured with the Clover detector, these effects have been investigated by GEANT4 simulations, assuming a conservative 20% uncertainty for the resulting corrections.

The SACS values $\sigma_{i,\,\rm exp}$ for the investigated isotopes i obtained from Eq. (7) represent an average over the quasistellar neutron spectrum used for the irradiation and can also be expressed as

$$\sigma_{i,\,\rm exp} = \frac{\int \sigma(E)\phi(E)dE}{\int \phi(E)dE}, \quad (8)$$

where $\sigma(E)$ is the differential cross section and $\phi(E)$ the experimental spectrum described in Sec. II A. This relation is later used for comparison with evaluated data and for deriving the respective MACS values.

IV. RESULTS

The following discussion concentrates on the comparison with experimental data. Tables of the related uncertainties are added for each isotope pair and a separate, explicit discussion of uncertainties follows in Sec. IV B.

A. Experimental (n,γ) cross sections

1. ^{174}Yb and ^{176}Yb

The results of the ten activations and the weighted average values are listed in Table III. As shown in Table IV the quoted accuracy is dominated by systematic uncertainties, in case of ^{176}Yb mostly by the intensities of the analyzed γ-ray transitions. For both isotopes the most accurate results were obtained in TOF measurements [27] with total uncertainties of about 2%. These data have been confirmed by the activations of this work within the quoted uncertainties of 2.8 and 7.3 % for ^{174}Yb and ^{176}Yb, respectively. A similarly good agreement is found with less accurate TOF data [28] after proper renormalization by the accepted ^{10}B(n,α) standard cross section [29], but obvious discrepancies exist compared to data reported in Ref. [30].

TABLE III. Results of the Yb activations.

Sample	Cross section [mb]	Uncertainty [%]
	^{174}Yb$(n,\gamma)^{175}$Yb	
Yb1	169	2.8
Yb2	164	2.9
Yb3	171	2.8
Yb4	168	2.9
Yb5	157	3.1
Yb6	160	3.0
Weighted average	165 ± 5	2.8
	^{176}Yb$(n,\gamma)^{177}$Yb	
Yb7	119.3	7.3
Yb8	123.4	7.3
Yb9	123.3	7.4
Yb10	113.0	7.4
Weighted average	120 ± 9	7.3

2. ^{190}Os and ^{192}Os

The activations on osmium exhibit perfect internal consistency and are significantly more accurate than previous data (Tables V and VI). For ^{190}Os, there is good agreement with the TOF measurement of Ref. [31], which quotes a significantly larger uncertainty of 15%. Earlier activation data [32,33] are far too high to be compatible with this work, even within their 10–15 % uncertainties. The situation for ^{192}Os is reversed, there is fair agreement with the activation of result of Ref. [32], whereas the data of Ref. [31] are too high by a factor of two.

3. ^{196}Pt and ^{198}Pt

The cross section uncertainties for ^{196}Pt and ^{198}Pt could be reduced by a factor of two or more compared to most previous

TABLE IV. Uncertainties of the Yb activations (in %).

Source of uncertainty	^{174}Yb	^{176}Yb
Au cross section	1.40	1.40
Isotopic abundance	0.44	0.39
Detector efficiency	2.00	2.00
γ-ray intensity	1.31–2.27	6.86–10.73
γ-ray self-absorption	0.01–0.09	$\leqslant$0.15
Time factor f_b	0.01–0.02	0.12-0.18
Half-life	0.02	0.16
Counting statistics	0.06–2.83	0.86–7.42
Stoichiometry	negligible	negligible
Total uncertainty	2.8	7.3

TABLE V. Results of the Os activations.

Sample	Cross section [mb]	Uncertainty [%]
	^{190}Os$(n,\gamma)^{191}$Os	
Os1	272	4.0
Os2	275	4.2
Os3	261	4.1
Weighted average	269 ± 11	4.0
	^{192}Os$(n,\gamma)^{193}$Os	
Os1	156.5	4.2
Os2	153.4	4.3
Os3	152.6	4.2
Weighted average	154 ± 6	4.2

data (Tables VII and VIII). For both isotopes good agreement within uncertainties was obtained with a similar activation measurement by Beer *et al.* [34], but for ^{198}Pt evaluated data by Allen *et al.* [36] can be ruled out as they are higher by a factor of two. In addition to the total (n,γ) cross sections, also the partial cross section feeding the $13/2^+$ isomer in ^{197}Pt with $t_{1/2} = 95$ min, which decays by two channels, via IT to the ground state (96.7%) and via β decay to ^{197}Au (3.3%), could be determined with significantly improved accuracy compared to Ref. [34]. Because of their short half-lives, the decay of the $5/2^+$ and $13/2^+$ isomers at 52.9 and 424 keV in ^{197}Pt and ^{199}Pt could not be identified in the present activations. As both isomers decay by internal transitions only, their partial cross sections are, therefore, included in the respective ground state values.

4. ^{202}Hg and ^{204}Hg

The ^{202}Hg cross section (Tables IX and X) was found to confirm the TOF data of Beer and Macklin [35], but the uncertainty could be improved by a factor of three. Results from other experiments are very discrepant and uncertain by 12 to 50 % [33,36]. No satisfactory solution could be obtained in the activation of ^{204}Hg due to the large uncertainty of 47% of the decay intensity I_γ. In this case, the TOF results of Ref. [35], which carry a 10% uncertainty, remain the only solid information for *s*-process applications.

TABLE VI. Uncertainties of the Os activations (in %).

Source of uncertainty	^{190}Os	^{192}Os
Au cross section	1.40	1.40
Isotopic abundance	negligible	negligible
Detector efficiency	2.00	2.00
γ-ray intensity	0.15	1.29
γ-ray self-absorption	0.10–0.20	0.01–0.02
Time factor f_b	0.07–0.12	0.04–0.07
Half-life	0.65	0.03
Counting statistics	0.14–0.22	0.21–0.34
Stoichiometry	3.13	3.13
Total uncertainty	4.0	4.2

TABLE VII. Results of the Pt activations.

Sample	Cross section [mb]	Uncertainty [%]
	^{196}Pt$(n,\gamma)^{197}$Pt	
Pt1	169.6[a]	11.1
Pt2	162.5[a]	11.1
Pt3	177.1[a]	11.1
Weighted average	169.4 ± 18.8[a]	11.1
β^--branch[b]	0.38 ± 0.01	2.6
Total (n,γ)	169.8± 18.8	
	^{196}Pt$(n,\gamma)^{197}$Pt^m	
Pt1	11.42	3.8
Pt2	11.14	4.6
Pt4	11.30	4.0
Weighted average		
IT branch	11.3 ± 0.4	3.8
β^- branch[b]	0.38 ± 0.01	2.6
Partial cross section	11.7 ± 0.4	3.7
	^{198}Pt$(n,\gamma)^{199}$Pt	
Pt1	97.69	4.4
Pt2	93.43	4.6
Pt4	93.08	4.4
Weighted average	94.7 ± 4.2	4.4

[a]Including IT branch of partial cross section to the $13/2^+$ isomer (corresponding to 96.7% of the partial cross section);
[b]β-decay branch to ^{197}Au corresponding to 3.3% of the partial cross section.

B. Uncertainties

In all activations the investigated samples had been sandwiched between gold foils of the same diameter, and the effective neutron flux was determined by averaging over the induced activities of the two gold foils. The samples were thin enough that self-shielding effects were almost negligible. The SACS value of ^{197}Au for the quasistellar spectrum used in this work was adopted from Ref. [11] ($\langle\sigma\rangle = 586 \pm 8$ mb) and contributes a systematic uncertainty of 1.4% in all cases.

The definition of the samples carries uncertainties due to the isotopic composition (adopted from the recommendations in Ref. [12]) and due to the stoichiometry in case of the Yb, Os, and Hg compounds (as specified by the supplier). For both

TABLE VIII. Uncertainties of the Pt activations (in %).

Source of uncertainty	^{196}Pt^m	^{196}Pt	^{198}Pt
Au cross section	1.40	1.40	1.40
Isotopic abundance	negligible	negligible	negligible
Detector efficiency	2.00	2.00	2.00
γ-ray intensity	2.70	10.81–14.51	0.85
GEANT simulations[a]	1.0–4.4	1.0–4.4	1.00
Time factor f_b	0.15	negligible	3.16–3.28
Half-life	0.19	negligible	1.30
Counting statistics	0.37–1.42	0.13–0.20	0.37–1.42
Total uncertainty	3.8	11.1	4.4

[a]including γ-ray self-absorption, coincidence summing, and effect of extended sample.

TABLE IX. Results of the Hg activations.

Sample	Cross section [mb]	Uncertainty [%]
	^{202}Hg$(n,\gamma)^{203}$Hg	
Hg1	63.20	4.0
Hg2	61.55	4.0
Hg3	62.81	4.0
Hg4	61.15	4.1
Hg5	61.58	4.2
Hg6	62.50	4.1
Weighted average	62.1 ± 2.5	4.0
	^{204}Hg$(n,\gamma)^{205}$Hg	
Hg7	33.52	46.9
Hg8	34.45	47.7
Hg9	30.23	47.9
Weighted average	32.5 ± 15.1	46.6

Os isotopes and ^{202}Hg the stoichiometry caused, in fact, the largest systematic uncertainty.

The uncertainty of the γ efficiency was determined by repeated calibrations in order to include the effect of the sample position. From the reproducibility of the calibrations and the specifications of the standard γ sources a 2% uncertainty was assigned to ε_γ.

For half of the investigated reactions the γ-ray intensities represent the main contribution to the systematic uncertainties. Especially for ^{204}Hg—and to a lesser extent for ^{176}Yb and ^{196}Pt—the uncertainties of the γ-ray intensities prevent an accurate determination of the cross sections by the activation technique.

While the corrections for γ-ray self-absorption are of minor importance, the time factors f_b show non-negligible uncertainties for ^{198}Pt and ^{204}Hg, because the irradiation times were about three times longer than the half-lives in these cases. The half-lives of the reaction products were not contributing to the uncertainty budget in general, although the effect exceeded the 1% level for ^{199}Pt and ^{205}Hg. Counting statistics were always good enough not to affect the final uncertainties. Even in the worst case of the ^{204}Hg cross section it contributed only about 6% compared to a total uncertainty of 47%.

In summary, it is important to note that the results of repeated activations with modified experimental conditions were always compatible with the quoted uncertainties. This provides evidence that the uncertainties were evaluated in a consistent and realistic way.

TABLE X. Uncertainties of the Hg activations (in %).

Source of uncertainty	^{202}Hg	^{204}Hg
Au cross section	1.40	1.40
Isotopic abundance	0.11	0.10
Detector efficiency	2.00	2.00
γ-ray intensity	0.06	45.45
γ-ray self-absorption	0.01–0.04	0.05–0.08
Time factor f_b	negligible	3.41–4.09
Half-life	0.03	1.75
Counting statistics	0.41–0.75	8.82–12.70
Stoichiometry	3.13	3.13
Total uncertainty	4.0	46.6

TABLE XI. Upper limits (in keV) of the resolved resonance region in different databases.

Isotope	JEFF 3.0/A	JEFF 3.1	JENDL-4.0	ENDF/B-VII.1
^{174}Yb	4.31	–	3.0	–
^{176}Yb	3.04	–	5.00	–
^{190}Os	–	–	0.80	–
^{192}Os	–	–	0.24	–
^{202}Hg	–	4.52	4.52	4.52

V. MAXWELLIAN AVERAGED CROSS SECTIONS

The quasistellar neutron spectrum used in the activations corresponds closely but not perfectly to a Maxwellian-Boltzmann distribution with $kT = 25$ keV [11] due to the energy cutoff at $E_n = 106$ keV and the small differences shown in Fig. 1. The true MACS values are obtained via

$$\langle\sigma\rangle_{kT} = \frac{2}{\sqrt{\pi}} \frac{\int_0^\infty \sigma(E_n) E_n e^{-E_n/kT} dE_n}{\int_0^\infty E_n e^{-E_n/kT} dE_n}, \tag{9}$$

where E_n is the neutron energy and $e^{-E_n/kT}$ the Boltzmann factor. In this expression, the energy-differential (n,γ) cross section $\sigma(E_n)$ from data libraries has to be normalized with the present SACS values determined by activation as described below.

A. Evaluated cross sections from data libraries

Energy-differential cross sections $\sigma(E_n)$ were adopted from the data libraries JEFF 3.1, JENDL 3.3, or JENDL 4.0, and ENDF-B/VII.1. These data can be divided into the resolved (RRR) and unresolved (URR) energy region. The corresponding upper limits of the RRR containing the thermal cross section and the resolved resonances are summarized in Table XI. The evaluated cross sections, which were obtained via the online data library JANIS [37], are based on experimental resonance parameters and/or theoretical calculations with the Hauser-Feshbach (HF) statistical model. In case of ^{204}Hg, where evaluated cross sections are missing, the corresponding MACS values were derived from statistical model calculations with the NON-SMOKER code [38]. In all other cases, the RRR had been treated independently from this normalization in order to avoid inconsistencies with the usually well-determined thermal cross sections [39].

The relative contributions of the RRR are summarized in Table XII. As conservative uncertainties of 20% were assumed for these components, this resulted in significant uncertainties in the total MACS data, depending on the energy range covered by the RRR.

TABLE XII. Contribution of the resolved resonance region to the Maxwellian-averaged cross sections (in %) for kT = 5–100 keV.

kT [keV]	5	10	15	20	25	30	40	50	60	80	100
					^{174}Yb						
JEFF 3.0/A	39	18	11	7.2	5.4	4.3	3.0	2.2	1.8	1.3	1.0
JENDL-4.0	29	12	6.9	4.6	3.3	2.6	1.8	1.3	1.0	0.7	0.5
					^{176}Yb						
JEFF 3.0/A	28	12	7.2	4.9	3.6	2.9	2.0	1.5	1.2	0.9	0.7
JENDL-4.0	46	21	12	8.1	5.9	4.6	3.1	2.4	1.9	1.3	1.0
					^{190}Os						
JENDL-4.0	5.4	2.1	1.2	0.8	0.5	0.4	0.2	0.2	0.1	0.1	0.1
					^{192}Os						
JENDL-4.0	0.3	0.1	0.1	0	0	0	0	0	0	0	0
					^{202}Hg						
JEFF 3.1	55	29	18	12	9.0	7.0	4.5	3.2	2.4	1.5	1.1
JENDL-4.0	56	30	19	13	9.5	7.3	4.8	3.4	2.5	1.6	1.1
ENDF/B-VII.1	58	31	20	14	10	7.6	5.0	3.5	2.6	1.7	1.2

B. Calculation of Maxwellian-average cross sections

In a first step, the energy-differential cross sections were folded with the experimental spectrum,

$$\sigma_{\text{eval}} = \int \sigma(E_n)\Phi_{\text{exp}}(E_n)dE_n, \tag{10}$$

for direct comparison with the measured cross sections σ_{exp}. The corresponding ratios

$$F_{\text{norm}} = \frac{\sigma_{\text{exp}}}{\sigma_{\text{eval}}} \tag{11}$$

in Table XIII represent the normalization factors that must be applied to the evaluated data if these are to be used for extrapolation to lower and higher thermal energies.

According to the special treatment of the RRR, the MACS data were determined via

$$\langle\sigma\rangle_{kT} = \langle\sigma\rangle_{kT}^{RRR} + F_{\text{norm}}\langle\sigma\rangle_{kT}^{URR}. \tag{12}$$

This expression is equivalent to obtaining a Maxwellian average from the energy-differential cross section $\sigma(E_n)$ after only the URR has been modified:

$$\langle\sigma\rangle_{kT} = \frac{2}{\sqrt{\pi}}\left[\frac{\int^{RRR}\sigma(E_n)E_n e^{-E_n/kT}dE_n}{\int^{RRR+URR}E_n e^{-E_n/kT}dE_n} + \frac{\int^{URR}F_{\text{norm}}\sigma(E_n)E_n e^{-E_n/kT}dE_n}{\int^{RRR+URR}E_n e^{-E_n/kT}dE_n}\right]. \tag{13}$$

The final normalized Maxwellian averaged cross sections $\langle\sigma\rangle_{kT}$ are summarized in Table XIV for comparison with the recommended values of the KADoNiS compilation [29]. The uncertainties discussed in Sec. IV B for the measured cross sections were also adopted for the MACS values between kT = 20 and 30 keV, assuming that the extrapolation uncertainties in the immediate vicinity of kT = 25 keV were negligible. For lower and higher thermal energies, increasing uncertainties have been estimated from the difference in the energy dependencies of the available evaluations. The particular choice of the evaluated cross section used for extrapolation and a comparison to the MACS values based on previous experiments are summarized below.

Laboratory cross sections always refer to the ground state of the investigated nuclei, but under stellar conditions low-lying excited nuclear states are populated by the intense thermal photon bath. Therefore, corrections for the effect (n,γ) reactions on excited states may contribute to the effective stellar cross sections and are commonly considered by the stellar enhancement factor (SEF) discussed in Refs. [38,40,41]. The SEF values of Ref. [29] have been complemented in Table XIV with the population probabilities for the ground states, $X_{i^{\text{lab}}}$ [42]. In the temperature regime of the main s-process component, i.e., for thermal energies below 30 keV, these numbers indicate that significant corrections for the effect of thermally populated excited states have to be considered only for ^{174,176}Yb.

TABLE XIII. Normalization factors $F_{\text{norm}} = \sigma_{\text{exp}}/\sigma_{\text{eval}}$ for adjusting the evaluated cross sections in the URR. The list includes the the results obtained with the pure Hauser-Feshbach (HF) statistical model code NON-SMOKER [38].

Isotope	JEFF 3.1	JENDL 4.0	ENDF-B/VII.1	NON-SMOKER
^{174}Yb	0.91[a]	0.99	–	0.98
^{176}Yb	1.03[a]	0.95	–	1.03
^{190}Os	–	0.78	–	1.29
^{192}Os	–	0.68	–	1.29
^{196}Pt	–	–	–	1.03
^{198}Pt	–	–	–	1.40
^{202}Hg	0.73	0.73	0.73	1.31
^{204}Hg	0.76	0.76	0.76	2.21

[a]Values from version JEFF 3.0/A.

C. Comparison with previous data and evaluations

The following comparison of the MACS values with previous results quoted in the KADoNiS compilation [29] is limited to a thermal energy of kT = 30 keV for better clarity. Note, that the original data may have been renormalized in some cases as indicated in [29].

1. MACS of Yb isotopes

The MACS calculations for the Yb isotopes have been performed using the energy-dependent cross section from the JEFF-3.0/A and JENDL-4.0 libraries. The MACS results in Table XIV are the average of the values obtained with the two evaluated data sets, assuming the respective differences as additional systematic uncertainties for the extrapolation to lower and higher temperatures. For both isotopes the MACS values are in very good agreement with the accurate TOF data from Ref. [27], which reported values at kT = 30 keV of 150.5 ± 1.8 and 115.9 ± 2.0 mb for ^{174}Yb and ^{176}Yb, respectively, thus confirming the coherence between the different experimental methods.

TABLE XIV. MACS values, stellar enhancement factors (SEF) [42], and ground state population ($X_{i\text{lab}}$), for thermal energies between $5 \leqslant kT \leqslant 100$ keV.

	Maxwellian averaged cross section (mb)										
kT [keV]	5	10	15	20	25	30	40	50	60	80	100
					^{174}Yb$(n,\gamma)^{175}$Yb						
This work	403(37)	280(16)	230(10)	198(8)	175.3(6.5)	157.5(5.7)	131.2(4.6)	112.7(3.7)	99.1(3.6)	80.5(3.2)	68.8(3.0)
Ref. [29]	374	271	220	190	168	151 (2)	125	108	95	78	67
SEF [29]	1.00	1.00	1.01	1.05	1.09	1.13	1.22	1.30	1.38	1.52	1.65
$X_{i\text{lab}}$ [42]	1.00	1.00	0.96	0.86	0.74	0.63	0.47	0.36	0.29	0.20	0.15
					^{176}Yb$(n,\gamma)^{177}$Yb						
This work	301(63)	204(28)	166(16)	143(12)	127(10)	114 (9)	95(9)	81(8)	69(8)	57(7)	48(6)
Ref. [29]	295	213	172	147	129	116 (2)	96	82	72	58	50
SEF [29]	1.00	1.00	1.01	1.04	1.08	1.12	1.20	1.28	1.36	1.51	1.65
$X_{i\text{lab}}$ [42]	1.00	1.00	0.97	0.89	0.78	0.67	0.50	0.39	0.31	0.21	0.16
					^{190}Os$(n,\gamma)^{191}$Os						
This work	662	442	362	321	296(12)	278 (11)	254	235	220	195	175
Ref. [29]	679	451	367	322	294	274 (12)	246	226	210	185	165
SEF [29]	1.00	1.00	1.00	1.00	1.00	1.01	1.02	1.05	1.08	1.15	1.22
$X_{i\text{lab}}$ [42]	1.00	1.00	1.00	1.00	1.00	0.98	0.93	0.85	0.76	0.58	0.45
					^{192}Os$(n,\gamma)^{193}$Os						
This work	367	248	205	183	169(7)	160 (7)	146	136	127	113	101
Ref. [29]	647	487	413	367	335	311 (45)	276	252	234	208	109
SEF [29]	1.00	1.00	1.00	1.00	1.00	1.00	1.01	1.02	1.04	1.08	1.13
$X_{i\text{lab}}$ [42]	1.00	1.00	1.00	1.00	1.00	0.99	0.96	0.90	0.82	0.66	0.52
					^{196}Pt$(n,\gamma)^{197}$Pt						
This work	452	295	236	204	185(20)	171 (19)	153	142	134	123	114
Ref. [29]	485	316	253	219	198	183 (16)	164	152	144	132	122
SEF [29]	1.00	1.00	1.00	1.00	1.00	1.00	1.00	1.00	1.01	1.02	1.04
$X_{i\text{lab}}$ [42]	1.00	1.00	1.00	1.00	1.00	1.00	1.00	0.99	0.98	0.92	0.83
					^{198}Pt$(n,\gamma)^{199}$Pt						
This work	287	177	137	116	103(4)	94 (4)	83	76	71	64	60
Ref. [29]	282	174	134	114	101	92 (5)	81	75	70	63	59
SEF [29]	1.00	1.00	1.00	1.00	1.00	1.00	1.00	1.00	1.00	1.01	1.01
$X_{i\text{lab}}$ [42]	1.00	1.00	1.00	1.00	1.00	1.00	1.00	1.00	0.99	0.96	0.91
					^{202}Hg$(n,\gamma)^{203}$Hg						
This work	185(25)	115(10)	90.0(6.4)	77.4(4.8)	68.9(3.8)	63.3(3.4)	56.0(2.8)	51.4(2.1)	48.2(2.1)	43.8(1.9)	40.7(1.7)
Ref. [29]	159	107	87	75	68	63 (2)	56	52	49	45	41
SEF [29]	1.00	1.00	1.00	1.00	1.00	1.00	1.00	1.00	1.00	1.00	1.00
$X_{i\text{lab}}$ [42]	1.00	1.00	1.00	1.00	1.00	1.00	1.00	1.00	1.00	0.98	0.94
					^{204}Hg$(n,\gamma)^{205}$Hg						
This work	75	54	44	39	35(16)	32 (15)	29	27	25	23	21
Ref. [29]	98	71	58	51	46	42 (4)	38	35	33	30	28
SEF [29]	1.00	1.00	1.00	1.00	1.00	1.00	1.00	1.00	1.00	1.00	0.99
$X_{i\text{lab}}$ [42]	1.00	1.00	1.00	1.00	1.00	1.00	1.00	1.00	1.00	0.98	0.95

2. *MACS of Os isotopes*

For ^{190,192}Os energy-dependent cross sections were available only from the JENDL-4.0 library. Therefore, systematic uncertainties for the extrapolation to higher and lower values of kT are derived from the resonance information of Ref. [39].

The new MACS value for ^{190}Os is smaller than data from previous experiments. While two of these are still compatible within uncertainties (295 ± 45 mb [31] and 320 ± 36 mb [32], respectively), the third result of 358 ± 55 mb (extrapolated from the measured value at 23 keV) is somewhat out of range [33]. In case of ^{192}Os, there is no acceptable agreement with the TOF measurement of Ref. [31], which is actually a factor of two higher (311 ± 15 mb) than the present MACS. Good agreement is still found with the result of the activation measurement of Ref. [32] (144 ± 15 mb).

3. *MACS of Pt isotopes*

For ^{194}Pt and ^{196}Pt, energy-dependent cross sections have been used from the theoretical work of Ref. [38], because the respective evaluations are missing in the data libraries. Accordingly, it was assumed that the systematic uncertainties

for the extrapolation to lower and higher kT values are gradually increasing to 20% at 5 and 100 keV.

Experimental differential neutron capture cross sections of ^{196}Pt have recently been reported by Koehler and Guber [43], yielding a MACS value of 167.4 ± 5.2 mb for $kT = 30$ keV, in excellent agreement with the present result. The value of 197 ± 23 mb from an earlier activation [34] is somewhat higher, but compatible within the quoted uncertainties.

For ^{198}Pt, the only other experimental value of 82 ± 12 mb was obtained in the activation work of Ref. [34]; again the difference of about 10% is within the range of uncertainties.

4. MACS of Hg isotopes

For ^{202}Hg and ^{204}Hg, the neutron energy-dependent cross sections from three databases, JEFF 3.1, JENDL 4.0, and ENDF/B-VII.1 have been used for the MACS calculations. Because the results are practically identical, the final MACS data of ^{202}Hg and ^{204}Hg at $kT = 30$ keV are based on the respective averages. The quoted uncertainties for the extrapolation to lower and higher kT values are based on the resonance information of Ref. [39].

The new MACS value at $kT = 30$ keV of 62 ± 2 mb for ^{202}Hg is significantly smaller than the 74 ± 6 mb from Ref. [35], which was determined using the TOF method.

The present activation for ^{204}Hg suffers from the large uncertainty of the γ-line intensity in the decay of ^{205}Hg and is, therefore, too uncertain for a meaningful comparison. Accordingly, the TOF value of 42 ± 4 mb quoted in Ref. [35] remains the best choice, unless the γ decay of ^{205}Hg can be significantly improved.

D. Trends with neutron number and astrophysics

The variation of the MACS values along isotopic chains is of twofold interest. In general, the development of average cross sections with neutron number represents a viable test for the global parameter sets used in large-scale HF calculations. Such calculations [38,44] are indispensable for studies of explosive nucleosynthesis, where the reaction paths of the r and p processes are shifted from the valley of stability towards the n-rich and p-rich regions, respectively. For the necessary extrapolation of the respective HF parameters the trends with neutron number illustrated in Fig. 5 provide useful information on sometimes surprising effects.

The plot of Fig. 5 compares the present results for $kT = 30$ keV with the recommended values in the KADoNiS compilation [29] (shaded areas corresponding to upper and lower bounds) and with the statistical model calculations using the NON-SMOKER code [38] (dashed lines). Because a preliminary version of the data set reported here had been already considered in KADoNiS, the respective differences are marginal. Therefore, the focus in Fig. 5 is on the direct comparison between the experiment-based data of KADoNiS and the values calculated with the NON-SMOKER code [38]. While the case of the Yb isotopes shows reasonably good agreement (apart from the 40% difference for ^{168}Yb), the data for Os exhibit significant deviations from a smooth

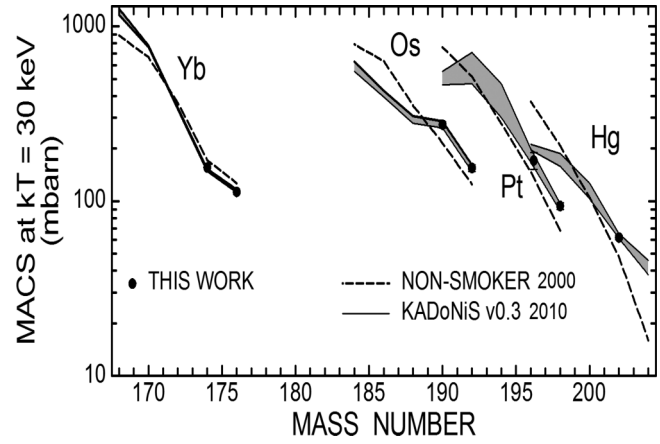

FIG. 5. Present experimental MACS values at $kT = 30$ keV for the even-even nuclei compared to the KADoNiS compilation (KADoNiS 2010: [29], shaded areas corresponding to upper and lower bounds of the recommended values) and to statistical model calculations with the NON-SMOKER code (NON-SMOKER 2000: [38], dashed lines).

decrease with neutron number as a consequence of local nuclear structure effects.

For the Pt sequence, the rather uncertain MACS values for ^{192,194}Pt in Ref. [29] have been replaced by the recent values from Koehler and Guber [43] to define the shaded area. For ^{194}Pt, there is perfect agreement with the present activation value. The new MACS for ^{190}Pt is higher than the value of Ref. [45], which had been obtained with the same activation technique, possibly due to the rather large uncertainties for the γ-line intensities in the decay of ^{191}Pt.

Finally, the experiment-based mercury sequence exhibits a significantly flatter trend than obtained in the NON-SMOKER calculations, which may have overestimated the effect of the nearby magic neutron number $N = 126$.

The impact of the present MACS data on the s-abundance pattern in solar material and in low metallicity stars was considered in a series of papers by Bisterzo *et al.* [46–48] via the preliminary values already included in the KADoNiS compilation. Accordingly, their results for the s abundances and the corresponding r residuals remain valid because the differences to the final results presented here are marginal.

The present results are important for MACS predictions of the neutron-rich isotopes involved in the s-process networks of the high neutron-density scenarios. This concerns AGB stars of intermediate mass (4–8 solar masses), where maximum temperatures of about 3.5×10^8 K are leading to a substantial neutron production via the ^{22}Ne$(\alpha,n)^{25}$Mg reaction. However, the s-process efficiency in these stars is much smaller than in low-mass AGBs stars, resulting in fairly low s abundances. A more important scenario are low-mass AGB stars of very low metallicity, where during the first thermal pulse the convective He layer expands over the H shell, thus engulfing protons from the envelope, which are instantly captured by the abundant ^{12}C in the convective region [49]. The ^{13}C produced in this way boosts the neutron density via the ^{13}C$(\alpha,n)^{16}$O reaction in addition to the ^{22}N$(\alpha,n)^{25}$Mg reaction at the bottom of the thermal pulse. First studies of this mechanism by Cristallo

et al. [49] have shown that neutron densities of 10^{15} cm^{-3} are reached during that phase, shifting the s-process path by a few mass units into the region of β instability. In this context, the present results are valuable for constraining the highly uncertain theoretical extrapolation of the MACS data required for this neutron-rich scenario [50].

VI. SUMMARY

The stellar (n,γ) cross sections of ^{174}Yb, ^{176}Yb, ^{190}Os, ^{192}Os, ^{196}Pt, ^{198}Pt, ^{202}Hg, and ^{204}Hg have been determined by a series of activation measurements, using the ^{7}Li$(p,n)^{7}$Be reaction for production of a quasistellar neutron spectrum at 25 keV thermal energy. The MACS values at $kT = 30$ keV of the above isotopes were found to be 157 ± 6 mb, 114 ± 10 mb, 278 ± 12 mb, 160 ± 7 mb, 171 ± 19 mb, 94 ± 4 mb, 62 ± 2 mb, and 32 ± 15 mb, respectively. In case of ^{196}Pt a partial cross section has been determined (11.4 ± 0.5 mb).

The majority of the cross sections are in good agreement with previous results. Particularly the values for ^{174}Yb and ^{176}Yb agree very well to previous data measured by means of the TOF method, thus confirming the coherence between the two experimental techniques.

The systematic uncertainties have been derived from repeated runs, which were carried out under different experimental conditions. Most new Maxwellian averaged cross sections have substantially smaller uncertainties than earlier data, especially for ^{190}Os, ^{192}Os, ^{198}Pt, and ^{202}Hg. In a few cases the uncertainties could not be reduced due to large uncertainties of the respective γ-line intensities, i.e., for ^{176}Yb, ^{196}Pt, and especially for ^{204}Hg.

Based on the activation results, MACS values were calculated for thermal energies between 5 and 100 keV. The respective energy-dependent cross sections for these calculations were obtained by normalizing evaluated or theoretical cross sections to the measured data. The present results for the stable neutron-rich isotopes are complementing previous measurements, thus providing the trend of the MACS values along the isotopic chains of Yb, Os, Pt, and Hg. The comparison with statistical model calculations indicates problems in using the HF approach with a global parameter set for extrapolation to the neutron-rich as well as to the proton-rich side of the stability valley. These problems might be alleviated by means of the new information.

The effect of the present MACS data on the s-abundance pattern in solar material and in low metallicity stars are confirming earlier s-process studies [46–48], which had been using preliminary values of this work from the KADoNiS compilation [29]. The present MACS data are also important for s-process scenarios characterized by high neutron densities, e.g. for intermediate mass AGB stars and, particularly, for the very strong flux during the first thermal instability in low-mass AGB stars of very low metallicity [49].

ACKNOWLEDGMENTS

We thank M. Brock, E.-P. Knaetsch, D. Roller, and W. Seith for their support during the irradiations at the Van de Graaff accelerator. We thank also E. Uberseder for his help with the GEANT4 simulations. J.M. is indebted to Karlsruhe Institute of Technology for financial support, and I.D. acknowledges support by the Helmholtz association under Contract No. VH-NG 627.

[1] E. Burbidge, G. Burbidge, W. Fowler, and F. Hoyle, Rev. Mod. Phys. **29**, 547 (1957).
[2] R. Gallino, C. Arlandini, M. Busso *et al.*, Astrophys. J. **497**, 388 (1998).
[3] F. Käppeler, R. Gallino, S. Bisterzo, and W. Aoki, Rev. Mod. Phys. **83**, 157 (2011).
[4] C. Arlandini, F. Käppeler, K. Wisshak *et al.*, Astrophys. J. **525**, 886 (1999).
[5] S. Bisterzo, F. Käppeler, R. Gallino *et al.*, in *Nuclei in the Cosmos-IX*, Proceedings of Science, SISSA, 2006, edited by A. Mengoni *et al.*, contribution 077 (SISSA, Trieste, 2006), http://pos.sissa.it/
[6] C. Freigburghaus, S. Rosswog, and F.-K. Thielemann, Astrophys. J. **525**, 121 (1999).
[7] K.-L. Kratz, K. Farouqi, B. Pfeiffer *et al.*, Astrophys. J. **662**, 39 (2007).
[8] A. Arcones and G. Martinez-Pinedo, Phys. Rev. C **83**, 045809 (2011).
[9] R. Reifarth, C. Lederer, and F. Käppeler, J. Phys. G: Nucl. Part. Phys. **41**, 053101 (2014).
[10] H. Beer and F. Käppeler, Phys. Rev. C **21**, 534 (1980).
[11] W. Ratynski and F. Käppeler, Phys. Rev. C **37**, 595 (1988).
[12] M. Berglund and M. E. Wieser, Pure Appl. Chem. **83**, 397 (2011).
[13] M. Shamsuzzoha Basunia, Nucl. Data Sheets **102**, 719 (2004).
[14] F. Kondev, Nucl. Data Sheets **98**, 801 (2003).
[15] V. Vanin, N. L. Maidana, R. M. Castro *et al.*, Nucl. Data Sheets **108**, 2393 (2007).
[16] E. Achterberg, O. A. Capurro, G. V. Marti *et al.*, Nucl. Data Sheets **107**, 1 (2006).
[17] X. Huang and C. Zhou, Nucl. Data Sheets **104**, 283 (2005).
[18] S. Singh, Nucl. Data Sheets **108**, 79 (2007).
[19] F. Kondev, Nucl. Data Sheets **105**, 1 (2005).
[20] F. Kondev, Nucl. Data Sheets **101**, 521 (2004).
[21] Z. Chunmei, Nucl. Data Sheets **95**, 59 (2002).
[22] S. Dababneh, N. Patronis, and P. A. Assimakopoulos *et al.*, Nucl. Instrum. Methods Phys. Res. A **517**, 230 (2004).
[23] S. Agostinelli, J. Allison, K. Amako *et al.*, Nucl. Instrum. Methods Phys. Res. A **506**, 250 (2003).
[24] W. R. Dixon, Nucleonics **8**, **4**, 68 (1951).
[25] NIST, technical report, National Institute of Standards and Technology, Online Access: http://www.nist.gov/pml/data/xraycoef/index.cfm.
[26] *Gamma- and X-Ray Spectrometry With Semi-conductor Detectors*, edited by K. Debertin and R. Helmer (North Holland, Amsterdam, 1989).
[27] K. Wisshak, F. Voss, C. Arlandini, F. Käppeler, and L. Kazakov, Phys. Rev. C **61**, 065801 (2000).

[28] V. Shorin, V. Kononov, and E. Poletaev, Yad. Fiz. **19**, 5 (1974).
[29] I. Dillmann, R. Plag, F. Käppeler, and T. Rauscher, in *EFNUDAT Fast Neutrons, Scientific Workshop on Neutron Measurements, Theory, and Applications*, edited by F.-J. Hambsch (Publications Office of the European Union, Luxembourg, 2010), p. 55, http://www.kadonis.org.
[30] M. Bokhovko, V. N. Kononov, E. D. Poletaev *et al.*, in *Nuclear Data for Science and Technology*, *Research Reports in Physics*, edited by S. Qaim (Springer, Berlin, 1992), p. 62.
[31] J. C. Browne and B. L. Berman, Phys. Rev.C **23**, 1434 (1981).
[32] T. Bradley, Z. Parsa, M. Stelts, and R. Chrien, in *Nuclear Cross Sections for Technology*, edited by J. L. Fowler, C. H. Johnson, and C. D. Bowman, Vol. 594 of NBS Special Publication (National Bureau of Standards, Washington DC, 1979), p. 344.
[33] K. Siddappa, M. Sriramachandra Murty, and J. Rama Rao, Nuovo Cimento A **18**, 48 (1973).
[34] H. Beer, P. Mohr, H. Oberhummer *et al.*, in *Interaction of Neutrons with Nuclei, ISINN–5*, edited by W. Furman (JINR, Dubna, 1997), p. 229.
[35] H. Beer and R. L. Macklin, Phys. Rev. C **32**, 738 (1985).
[36] B. Allen, J. Gibbons, and R. Macklin, Adv. Nucl. Phys. **4**, 205 (1971).
[37] JANIS, OECD Nuclear Energy Agency, Paris, http://www.nea.fr/janis/.
[38] T. Rauscher and F.-K. Thielemann, At. Data Nucl. Data Tables **75**, 1 (2000).
[39] S. F. Mughabghab, *Atlas of Neutron Resonances*, 5th ed. (Elsevier, Amsterdam, 2006).
[40] T. Rauscher, P. Mohr, I. Dillmann, and R. Plag, Astrophys. J. **738**, 143 (2011).
[41] T. Rauscher, Int. J. Mod. Phys. E **20**, 1071 (2011).
[42] T. Rauscher, Astrophys. J. Lett. **755**, L10 (2012).
[43] P. E. Koehler and K. H. Guber, Phys. Rev. C **88**, 035802 (2013).
[44] S. Goriely, technical report, http://www-astro.ulb.ac.be.
[45] J. Marganiec, I. Dillmann, C. Domingo Pardo *et al.*, Phys. Rev. C **79**, 065802 (2009).
[46] S. Bisterzo, R. Gallino, O. Straniero *et al.*, Mon. Not. Royal Astron. Soc. **404**, 1529 (2010).
[47] S. Bisterzo, R. Gallino, O. Straniero *et al.*, Mon. Not. Royal Astron. Soc. **418**, 284 (2011).
[48] S. Bisterzo, R. Gallino, O. Straniero *et al.*, Mon. Not. Royal Astron. Soc. **422**, 849 (2012).
[49] S. Cristallo, L. Piersanti, O. Straniero *et al.*, Publ. Astron. Soc. Australia **26**, 139 (2009).
[50] M. G. Bertolli, F. Herwig, M. Pignatari, and T. Kawano, arXiv:1310.4578v1.